Article

Engineering Single-Atom Electrocatalysts for Enhancing Kinetics of Acidic Volmer Reaction

Hao Cao,[¶] Qilun Wang,[¶] Zisheng Zhang, Hui-Min Yan, Hongyan Zhao, Hong Bin Yang, Bin Liu,* Jun Li, and Yang-Gang Wang*

Read Online

ACCESS | 📊 Metrics & More | 📇 Article Recommendations | 🔵 Supporting Information

ABSTRACT: The design of active and low-cost electrocatalyst for hydrogen evolution reaction (HER) is the key to achieving a clean hydrogen energy infrastructure. The most successful design principle of hydrogen electrocatalyst is the activity volcano plot, which is based on Sabatier principle and has been used to understand the exceptional activity of noble metal and design of metal alloy catalysts. However, this application of volcano plot in designing single-atom electrocatalysts (SAEs) on nitrogen doped graphene (TM/N_4C catalysts) for HER has been less successful due to the nonmetallic nature of the single metal atom site. Herein, by performing ab initio molecular dynamics simulations and free energy calculations on a series of SAEs systems (TM/N_4C with TM = 3d, 4d, or 5d metals), we find that the strong charge−dipole interaction between the negatively charged *H intermediate and the interfacial H_2O molecules could alter the transition path of the acidic Volmer reaction and dramatically raise its kinetic barrier, despite its favorable adsorption free energy. Such kinetic hindrance is also experimentally confirmed by electrochemical measurements. By combining the hydrogen adsorption free energy and the physics of competing interfacial interactions, we propose a unifying design principle for engineering the SAEs used for hydrogen energy conversion, which incorporates both thermodynamic and kinetic considerations and allows going beyond the activity volcano model.
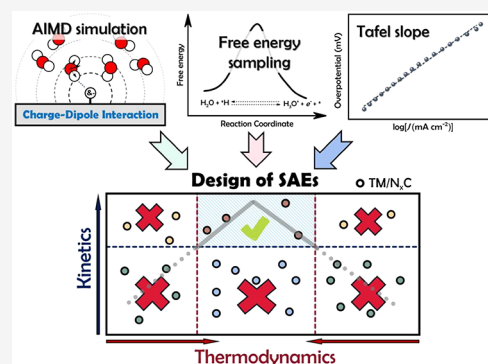
INTRODUCTION

The hydrogen evolution reaction (HER) is the key electrochemical process for the storage/utilization of hydrogen energy.[1,2] Mechanistic understanding of the elementary steps in HER is hence crucial for rational design of active hydrogen electrocatalysts.[3] In alkaline media, the HER rates are dramatically slower (2−3 orders of magnitude) than in acidic media, due to the sluggish kinetics of water dissociation and OH^- desorption.[4−8] In acidic media, with hydronium being the primary proton source, it has been hypothesized that the HER activity solely depends on the hydrogen binding energy (HBE) of the catalysts[9] and that an intermediate binding strength of *H leads to optimal performance according to the Sabatier principle; i.e., the interaction between adsorbate and substrate should not be too strong or too weak.[10] By combining density functional theory (DFT) calculations and computational hydrogen electrode (CHE) method, Nørskov and co-workers identified the "volcano-type" trend based on the relationship between HER exchange current density and free energy of Volmer reaction (i.e., ΔG_{*H}).[11,12] This relationship helps us understand the exceptionally high acidic HER activity of noble metal catalysts, such as Pt, Pd, Ir, etc.,[11] and the apex of the volcano curve has an instructive significance for further optimizing metal HER catalysts by alloying or doping.[13,14]

Among emerging classes of HER catalysts, the two-dimensional (2D) single-atom electrocatalysts (SAEs), such as the isolated metal atoms anchored on nitrogen-doped graphene, are born with many distinct advantages (e.g., high atomic efficiency, low cost, and well-defined active site),[15−17] encouraging a growing number of researchers to develop HER SAEs with high performance.[18−21] However, since the nature of the active sites in SAEs is more cationic than metallic and the adsorbed dihydrogen species could exist, the traditional "volcano" plot has been demonstrated to be less effective for designing SAEs for HER.[22] Based on Hossain et al.'s report, the Fe/N_4C and Cr/N_4C are predicted to present good HER catalytic activity with the ΔG_{*H} in the range of −0.20 to 0.30 eV, while the experimental overpotential of Fe/NC is as large as ∼0.5 V, showing the inconsistency with theoretical prediction.[23,24] Therefore, the development of more precise descriptors other than the simple ΔG_{*H} is imminent for the design of advanced HER SAEs. Additionally, the explicit

description of solvation environment is quite necessary in modeling electrocatalysis on SAEs, in terms of thermodynamics, kinetics, and even mechanistic pathways.[25−27] Overlooking the interaction between adsorbates and solvent (e.g., hydrogen bonding) at electrochemical interface during ab initio calculation may receive unstable reaction intermediates and induce the obvious discrepancy between theoretical predictions and experimental data.[28−30]

In this work, we perform ab initio molecular dynamics (AIMD) and constrained AIMD simulations with explicit solvation model to investigate the kinetics of acidic Volmer reaction on TM/N_4C (TM = Cr, Mn, Fe, Co, Ru, Ir, Rh). The thermodynamic integration (TI) method and charge-extrapolation scheme are employed to acquire the constant-potential free energy profiles of Volmer reaction on the SAEs. We observe a special configuration of interfacial H_2O molecules around the negative charged *H intermediate adsorbed on Cr/N_4C, Mn/N_4C, and Fe/N_4C systems, with one H in H_2O pointing to the *H (*H···HOH). This is because of the strong charge−dipole interaction between *H and interfacial H_2O molecules, and this effect also alters the transition path of the acidic Volmer reaction, increasing its kinetic barrier. The kinetic bottleneck of Volmer reaction on Cr/N_4C is the most significant on the studied systems since its *H is more negatively charged than those of Mn/N_4C and Fe/N_4C. Such kinetic hindrance is also confirmed by the experimental HER activity test and Tafel slope. We thus propose a design principle that incorporates the physics of interfacial interaction for improved description of acidic HER kinetics on TM/N_xC materials. The "volcano-like" relationship between thermodynamic and kinetic descriptors is built, which identifies the applicability of traditional "volcano" plot on different SAEs and offers a direction for reducing the kinetic influence via coordination engineering on HER.

■ METHODS

Computational Models. The TM/N_4C substrates were modeled by a single layer of four nitrogen atom-doped graphene with a single transition metal (TM) atom embedded in the center (Figure S1). The slabs were composed of a 6 × 4 supercell with dimensions of 17.04 × 14.76 × 20.00 Å^3 and was allowed to repeat periodically. For the calculation of free energy barrier, the liquid models were built where the empty spaces of the simulation box were filled with bulk water, containing 141 H_2O molecules and possessed an average density of ~1 g/cm^3.

Computational Parameters. The spin-polarized DFT calculations[31] were performed by adopting the Vienna ab initio simulation package (VASP) code.[32] The exchange−correlation energy was described by the generalized-gradient approximation (GGA) with Perdew−Burke−Ernzerh (PBE) functional.[33] The valence states of all atoms were expanded in a plane-wave basis set with a cutoff energy of 400 eV. The 3 × 3 × 1 K-point sampling of the Brillouin zone was set. The implicit solvation effect was also introduced by VASPsol.[34]

The free energy of hydrogen adsorption (ΔG_{*H}) via computational hydrogen electrode (CHE) model[35] is calculated by the eqs 1 and 2:

$$\Delta E_{*H} = E_{*H} - E_* - \frac{1}{2}E_{H2} \tag{1}$$

where E_{*H} is the total energy of catalyst surface with hydrogen adsorption, E_* is the energy of clean catalyst surface and E_{H2} is the energy of hydrogen molecule.

$$\Delta G_{*H} = \Delta E_{*H} + \Delta E_{ZPE} - T\Delta S \tag{2}$$

where ΔE_{ZPE} is the zero-point energy correction and $T\Delta S$ is the change in the entropy contribution to the free energy.

The ab initio molecular dynamics (AIMD) simulations and constrained MD simulations were performed by employing the CP2K/Quickstep package.[36] The Perdew−Burke−Ernzerhof (PBE) functional and mixed double-ζ Gaussian and plane-wave (GPW) basis sets with an energy cutoff of 400 Ry are chosen.[33] The core electrons of different element were modeled by the Goedecker−Teter−Hutter (GTH) pseudopotentials. The AIMD simulations were sampled by the canonical (NVT) ensemble using Nose−Hoover thermostats with the target temperature of 300 K, and the time step is set as 1.0 fs.[37,38] In all the calculations, the DFT-D3 method proposed by Grimme et al. was adopted to better describe the noncovalent interactions.[39]

The kinetic barriers of Volmer reaction ($H_3O^+ + e^- + * = *H + H_2O$) on TM/N_4C (TM = Cr, Fe, Co, Rh) are obtained by thermodynamic integration (TI) method which applies a holonomic constraint on reaction coordinate (ζ) during MD simulations and integrate over the average unbiased force associated with the reaction coordinate eq 3,[40,41]

$$\Delta A(\zeta) = -\int_{\zeta_a}^{\zeta_b} F(\zeta)\, d\zeta \tag{3}$$

where $\Delta A(\zeta)$ is the free energy difference between two reaction coordinates (ζ_a and ζ_b) and $F(\zeta)$ is the averaged force along the constrained reaction coordinate. The collective variable (CV) is defined by eq 4,

$$CV = \zeta(\mathbf{r}) = |\mathbf{r}_{TM} - \mathbf{r}_H| - |\mathbf{r}_O - \mathbf{r}_H| \tag{4}$$

where r_{TM} refers to the coordinates of transition metal atom, r_O refers to the coordinates of O atom on H_3O^+, and $\mathbf{r}_H$ refers to the coordinate of solvated proton on H_3O^+ (Figure S1).

Synthesis of TM-Based SAEs. In a typical synthesis of Cr_1/NC, a mixture of melamine ($C_3H_6N_6$) (8 g), L-alanine ($C_3H_7NO_2$) (1.5 g) and chromium(III) nitrate nonahydrate ($Cr(NO_3)_3·9H_2O$) (35 mg) were first ground into a uniform precursor by ball-milling for 1 h in a nylon jar. Subsequently, 12 mL of hydrochloric acid (HCl) and 3 mL of ethanol (C_2H_6O) were added and dried in an oven at 60 °C until the complete evaporation of ethanol. Then the fine powder mixture underwent a two-stage pyrolysis under Ar atmosphere. The first stage was from 25 to 600 °C at a ramping rate of 2.5 °C min^{-1} and held at 600 °C for 2 h, while the second stage was from 600 to 900 °C at a ramping rate of 2.5 °C min^{-1} and held at 900 °C for 1 h. After cooling to room temperature, the product was washed with 2 M HCl solution at 80 °C for 24 h to remove possible metal particles and annealed again at 900 °C under Ar. Fe/NC, Co/NC, and Rh/NC were synthesized by replacing $Cr(NO_3)_3·9H_2O$ with $Fe(CO_2CH_3)_2$, $Co(CO_2CH_3)_2$, and $RhCl_3·xH_2O$.

Characterization. The transmission electron microscopy (TEM) was measured on a JEOL JEM-2100F. Aberration-corrected high-angle annular dark-field scanning transmission electron microscopy (AC-HAADF-STEM) was conducted on a JEOL JEMARM200F STEM/TEM with a guaranteed resolution of 0.08 nm. The crystal structure was examined by X-ray diffraction (XRD, Bruker AXS D8 Advance) using Cu Kα radiation (λ = 1.5406 Å) with a LYNXEYE detector at 30 kV and 10 mA. The mass contents of metal in SAEs were quantified by inductively coupled plasma mass spectroscopy (ICP-MS, PerkinElmer). Detailed elemental compositions were analyzed by X-ray photoelectron spectroscopy (XPS) on an ESCALAB 250 photoelectron spectrometer (Thermo Fisher Scientific) using a monochromatic Al Kα X-ray beam (1486.6 eV). All binding energies were calibrated to the C 1s peak (284.6 eV) arising from the adventitious carbon-containing species.

Electrochemical Measurements. The electrochemical measurements were conducted at ambient temperature and pressure using a CHI 760e potentiostat. The 0.1 M $HClO_4$ electrolyte was prepared from appropriate 70 wt % double distilled $HClO_4$ with ultrapure water. During HER tests, the electrolyte was saturated with Ar (99.99%) by purging Ar into the aqueous 0.1 M $HClO_4$ solution for 30 min and then maintaining the flow of Ar throughout the entire electrochemical measurements. Electrocatalyst inks were prepared by dispersing 5 mg of catalyst into a solution containing 25 μL of 5 wt %
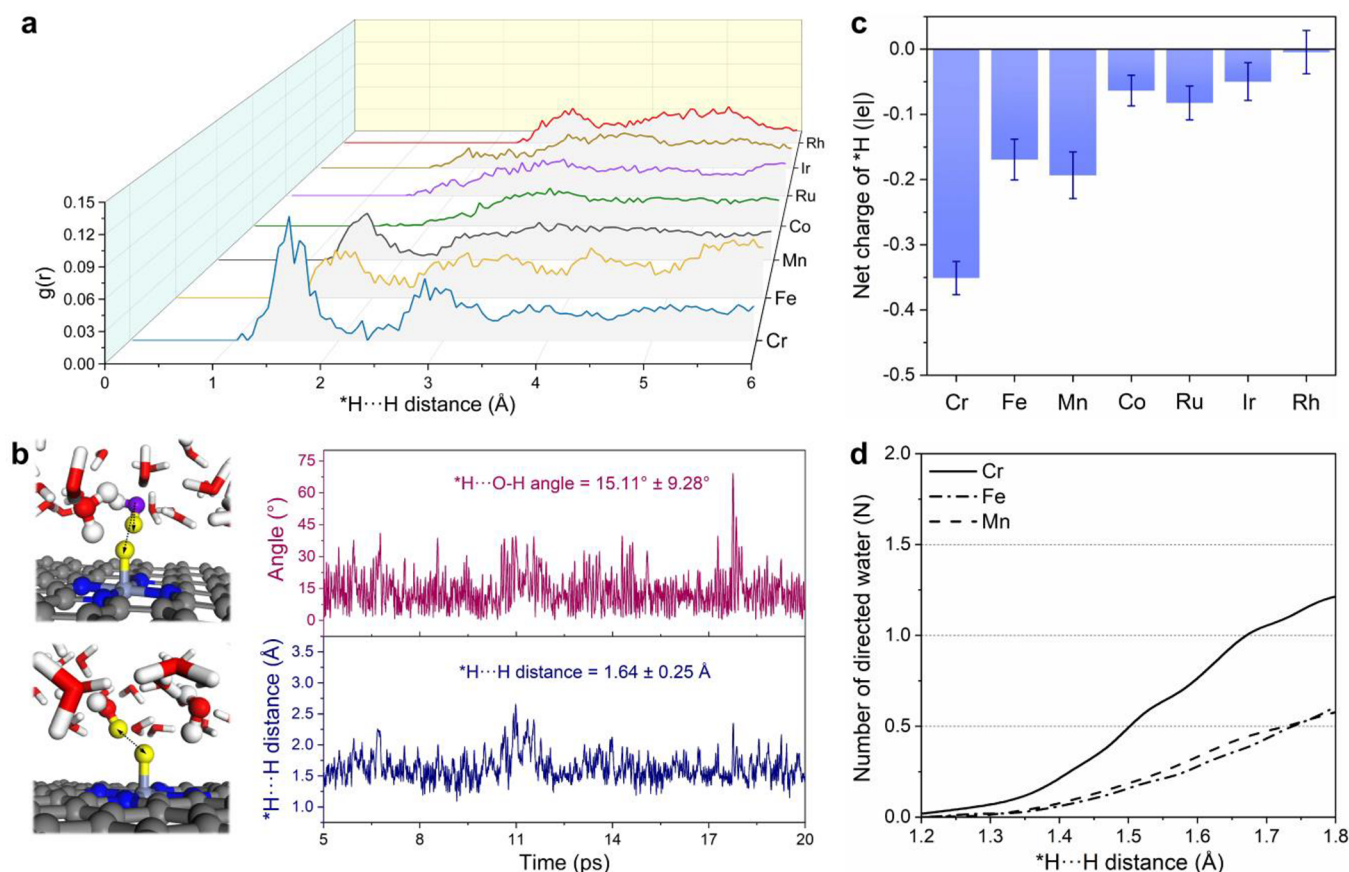
Figure 1. Ab initio molecular dynamics (AIMD) simulations for the adsorbed hydrogen (*H) on different TM/N$_4$C catalysts. (a) Radial distribution function (RDF) analysis of directed H$_2$O molecules around the *H in the sphere of *H⋯H distance on different catalysts. (b) Illustration and analysis of *H⋯O−H angle and *H⋯H distance on Cr−N$_4$-C catalyst during 5−20 ps AIMD simulation. (c) Averaged Bader charges of *H on different TM/N$_4$C catalysts during AIMD simulations. (d) Number of directed H$_2$O molecule in the *H⋯H distance range of 1.2−1.8 Å.

Nafion 117 solution (as conducting binder) and 975 μL of ultrapure water−isopropanol solution with equal volumes of water and isopropanol, followed by ultrasonication for 3 h. A three-electrode glass cell configuration was employed with a working electrode of glassy carbon rotating disk electrode (RDE) with 5 mm diameter, a counter electrode of graphite rod, and a saturated calomel electrode (SCE) as the reference electrode. Before each experiment, the glassy carbon electrode was polished to mirror shine with 0.05 μm alumina, then an aliquot of 12 μL of the catalyst ink was drop-casted on the glassy carbon electrode (catalyst loading: 0.3 mg cm^{-2}) and allowed to dry in air. All reported electrode potentials were referenced to the RHE scale as $E(vs\ RHE) = E(vs\ SCE) + 0.0591\ V \times pH + 0.2415\ V$. The overpotential η was calculated by $\eta = |E(vs\ RHE)|\ V$. Polarization curves were recorded at a scan rate of 5 mV s^{-1} with 100% solution ohmic drop correction under 1600 rpm. The reported current densities were normalized to the geometrical area of electrode (mA cm$_{geo}^{-2}$).

RESULTS AND DISCUSSION

AIMD Simulations for the Solvent−Adsorbate Structure. First, we screened the TM/N$_4$C SAEs for HER, using the traditional CHE model and with the ΔG_{*H} as the sole criteria (Figure S2). The calculations suggest that the Cr/N$_4$C, Fe/N$_4$C, Co/N$_4$C, and Rh/N$_4$C are the best candidates for HER, with their $|\Delta G_{*H}|$ smaller than 0.30 eV. However, this simple model fails to capture the explicit solvation effects during the electrochemical reaction, which are critical for the reaction activity.[42]

To consider the reaction kinetics and more realistically model the acidic Volmer reaction on TM/N$_4$C, we performed AIMD simulations on the water/H$_{ads}$-TM/N$_4$C interfaces with explicit solvation, each of 20 ps duration. Interestingly, we found that the H$_2$O molecules near the adsorbed hydrogen (*H) show strong orientational preference, and their spatial distribution depends on the identity of the metal center. Figure 1a presents the radial distribution function (RDF) analysis of *H⋯H distance on different models. An obvious peak in the range of 1.0−1.8 Å can be observed in H$_{ads}$-Cr/N$_4$C, H$_{ads}$-Mn/N$_4$C, and H$_{ads}$-Fe/N$_4$C but not in H$_{ads}$-Co/N$_4$C, H$_{ads}$-Ru/N$_4$C, H$_{ads}$-Ir/N$_4$C, and H$_{ads}$-Rh/N$_4$C. This suggests a *H⋯HOH motif at the catalyst/water interface on the former three systems, where one H atom in water points to the *H. This specific configuration can be confirmed by analyzing the *H⋯H distance and the angle of ∠*H⋯O−H. Figure 1b shows that the average *H⋯O−H angle and distance are ~15° and ~1.64 Å on H$_{ads}$-Cr/N$_4$C during simulation, respectively. To elucidate the origin of this specific configuration, we carried out Bader charge analysis to study the charge distribution on *H during the simulations. As shown in Figure 1c, although the *H in all cases is negatively charged, the amount of charge differs. The *H gains a significant number of electrons from Cr/N$_4$C surface (−0.35 |e| on average), indicating a hydridic feature. Similarly, the *H on H$_{ads}$-Mn/N$_4$C and H$_{ads}$-Fe/N$_4$C is also negatively charged by −0.19 |e| and −0.17 |e|, respectively. In the cases of Co, Rh, Ir, and Rh, the charge
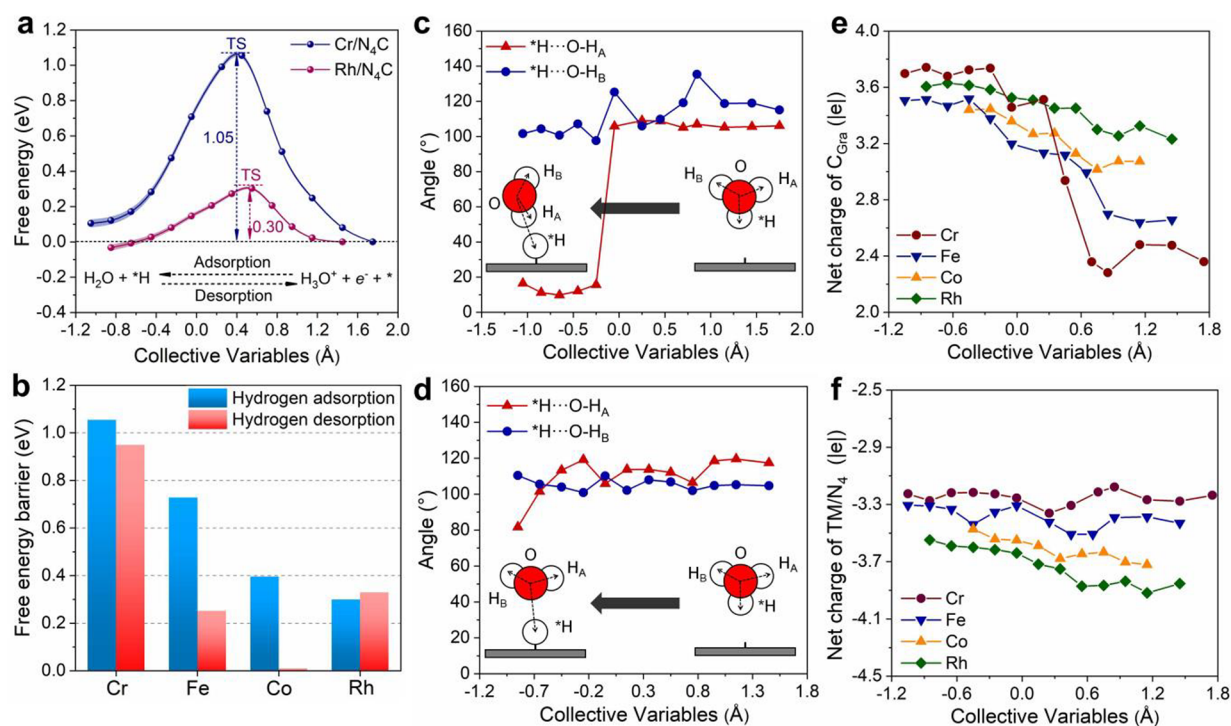
Figure 2. Thermodynamics/kinetics of Volmer reaction and analysis of reactant behavior during reaction. (a) Free energy profiles of Volmer reaction on Cr/N_4C and Rh/N_4C at PZC (-0.07 V vs SHE from experimental work[55]). The shaded area refers to the error bar of 95% confidence intervals based on standard errors. (b) Reactive free energy barrier of hydrogen adsorption and hydrogen desorption on different catalysts. (c, d) Analysis of angle between adsorbed hydrogen and O−H bond of water ($\angle*H\cdots O-H$) along the collective variables on (c) Cr/N_4C and (d) Rh/N_4C. (e, f) Evolution of net charges on (e) defective graphene surface (C_{gra}) and (f) TM/N_4 moiety for different catalysts.

on *H are within a much more positive range of -0.005 |e| to -0.10 |e|, showing an electroneutral feature. Thus, we believe that formation of the *H⋯HOH interfacial configuration results from the charge−dipole interaction between the negatively charged *H and the polar water molecule, as is illustrated in Figure S4. Moreover, the *H on H_{ads}-Cr/N_4C attracts and stabilizes more water molecules as compared to the case of Fe and Mn, which further reorganizes the local water structure near the active center (Figure 1d).

Kinetics of Volmer Reaction and Origin of Transferred Charge. We then investigated the free energy profiles of the interfacial *H⋯HOH configuration on the acidic Volmer reaction by constrained AIMD simulations combined with TI method to acquire the free energy profiles (FEP) of Volmer reaction on Cr/N_4C, Fe/N_4C, Co/N_4C, and Rh/N_4C.[29,43] Constant-potential corrections were added to the free energies to account for the shift in electrode potential as the collective variable (CV) varies (more details about TI and constant-potential methods are presented in Supporting Information).[44,45] As is shown in Figure 2a, the reaction free energy of hydrogen adsorption (ΔG_{*H_TI}) on Cr/N_4C and Rh/N_4C is only 0.10 eV and -0.04 eV at the potential of zero charge (PZC), suggesting that the hydrogen adsorption on these two catalysts is rather thermodynamically favorable, also consistent with the CHE model calculations. However, the free energy barriers ($\Delta G^{\ddagger}_{*H}$) on the two catalysts diverges, with a high barrier of 1.04 eV on Cr/N_4C and a low barrier of 0.30 eV on Rh/N_4C. Therefore, the hydrogen adsorption on Cr/N_4C is actually kinetically hindered and requires a higher overpotential to drive. Such kinetic hindrance is also observed on Fe/N_4C whose $\Delta G^{\ddagger}_{*H}$ reaches 0.75 eV, whereas the ΔG_{*H} is only 0.48 eV. In contrast, such kinetic limitation is not seen on

Co/N_4C whose ΔG_{*H} and $\Delta G^{\ddagger}_{*H}$ are 0.39 and 0.40 eV, respectively. The free energy barriers of hydrogen desorption at PZC on different SAEs are also summarized in Figure 2b. For the Cr/N_4C, the large barrier of 0.95 eV during desorption also means very low activity toward hydrogen oxidation. In summary, the kinetics and thermodynamics of acidic Volmer reaction are highly decoupled on TM/N_4C, and thermodynamics of hydrogen binding should not be used as the sole activity descriptor.

To understand the origin of the decoupling behavior, the geometric analysis of AIMD trajectories was performed on different SAEs. Figure 2c shows the variation of the *H⋯O−H_A and *H⋯O−H_B angle (H_A and H_B represent the different H atom of H_2O carrier) during the Volmer reaction on Cr/N_4C, where the angle of *H⋯O−H_B stays unchanged during reaction, but the angle of *H⋯O−H_A sharply decreases ($\sim90°$) as the system goes from initial state (IS) to final state (FS). The reorientation of the H_2O agrees with the RDF analysis on H_{ads}-Cr/N_4C as shown above and is also found in the case of Fe/N_4C (Figure S8a) despite a smaller variation in angle by $\sim30°$. In addition, Figure 2d and Figure S8b show that both *H⋯O−H_A and *H⋯O−H_B angles do not change much during Volmer reaction on Rh/N_4C and Co/N_4C, indicating the a robust orientational preference of the interfacial H_2O (O-down) along the reaction coordinate. Combined with the Bader charge analysis in the previous section (Figure 1c) as well as the relationship between $\angle*H\cdots O-H$ and the charge state of *H (Figure S9), we conclude that the orientation of H_2O carrier during Volmer reaction is dependent on the charge state of *H. As the hydrogen adsorption proceeds, the transferred proton would continuously accept charges from the catalyst's surface while
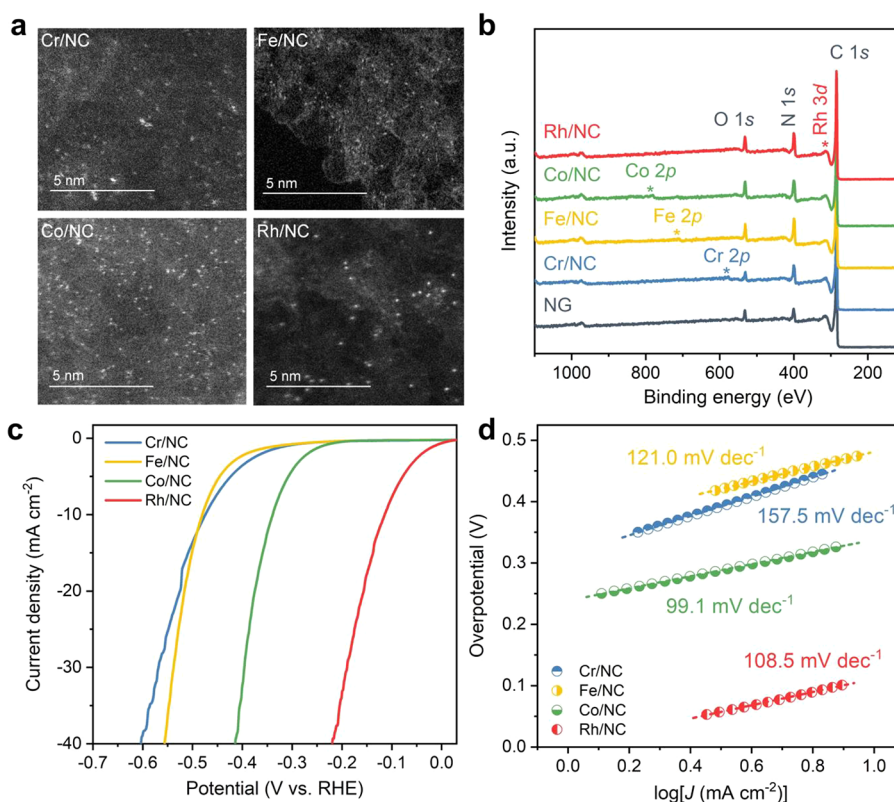
Figure 3. Structural characterizations and HER activities of SAEs. (a) AC-HAADF-STEM image of Cr/NC, Fe/NC, Co/NC, and Rh/NC. (b) Survey XPS spectra of all the as-synthesized TM/NC. The source of O is mostly related to the edge groups of N-doped graphene matrix as well as physically adsorbed and/or trapped oxygen and moisture. (c) HER polarization curves of different TM/NC acquired at a sweep rate of 5 mV s^{-1} in Ar-saturated 0.1 M HClO$_4$. All measurements were calibrated with *iR* compensation. Catalyst loading: 0.3 mg cm^{-2}. Rotation speed: 1600 rpm. (d) Tafel plots for different TM/NC.

approaching the metal center. For the Cr/N$_4$C, the *H gains enough negative charge (more than 0.14 |e|) to become hydridic, and the strong charge−dipole interaction between *H and H of H$_2$O would induce a significant configurational change of interfacial H$_2$O molecule. Such reorientation of interfacial H$_2$O orientation does not occur on Rh/N$_4$C since the close-to-zero net charge on its *H at FS. Likewise, for the hydrogen desorption process, the inverse reorientation (from *H···H direction to *H···O direction) is also necessary for the transfer of *H to H$_2$O to produce a free hydronium. In other words, the electronegativity of the metal center dictates the charge state of the *H, which then reshapes the free energy landscape of the Volmer reaction. As a result, the transition path of the Volmer reaction (whether interfacial water is reoriented) differs on different metals and breaks the Brønsted−Evans−Polanyi (BEP) relation.

To track the electron transfer during the reaction, we performed Bader charge analysis for each constrained MD trajectory and analyze the charge variation for different species. Figure 2e,f shows that the transferred charge primarily comes from the graphitic carbon matrix, especially for Cr/N$_4$C (1.30 |e|) and Fe/N$_4$C (0.86 |e|). The TM/N$_4$ moiety also transfers a small amount of charge, which is in the range of 0.01−0.31 |e| for CrN$_4$ to RhN$_4$ catalyst.

Experimental Characterization and HER Activity. To verify the proposed mechanism of kinetics-limited acidic HER performance of SAEs, a series of carbon-supported transition metal (TM)-based SAEs (Cr/NC, Fe/NC, Co/NC, and Rh/NC) were synthesized by pyrolyzing a homogeneous mixture

of melamine, L-alanine, and the corresponding metal salt.[46,47] The powder X-ray diffraction (XRD) patterns of all as-synthesized SAEs show a single broad peak at around 26.2°, which can be assigned to the graphite-like carbon (002) plane, suggesting a graphitic substrate with low-degree crystallinity (Figure S10). Moreover, the absence of metal, metal nitride, or metal oxide related diffraction peaks implies no metal-containing crystals in the SAE samples. In consistence with the XRD results, no particles can be observed in the high-resolution transmission electron microscopy (HRTEM) images, verifying high dispersion of metal species on the carbon matrix (Figure S11). The atomic-scale distributions of various metals are further confirmed by aberration-corrected high-angle annular dark-field scanning TEM (AC-HAADF-STEM) as isolated bright dots with an average diameter of about 0.2 nm (Figure 3a). To examine the chemical composition and coordination environment of SAEs, X-ray photoelectron spectroscopy (XPS) measurements were performed. Carbon, nitrogen, oxygen, and the corresponding metal elements are identified in the survey spectra, revealing the successful doping of nitrogen and metal atoms into carbon matrix (Figure 3b). As shown in Table S2, the metal contents in the four SAEs are nearly identical and estimated to be in the range of ~0.2−0.3 atom %, in line with the inductively coupled plasma mass spectroscopy (ICP-MS) measurements. Notably, the atomic percentages of N in the SAEs are among ~10−13 atom % and significantly higher than that in the pristine NC substrate (6.9 atom %), suggesting that the metal and nitrogen might stabilize each other. The high-resolution N 1s XPS
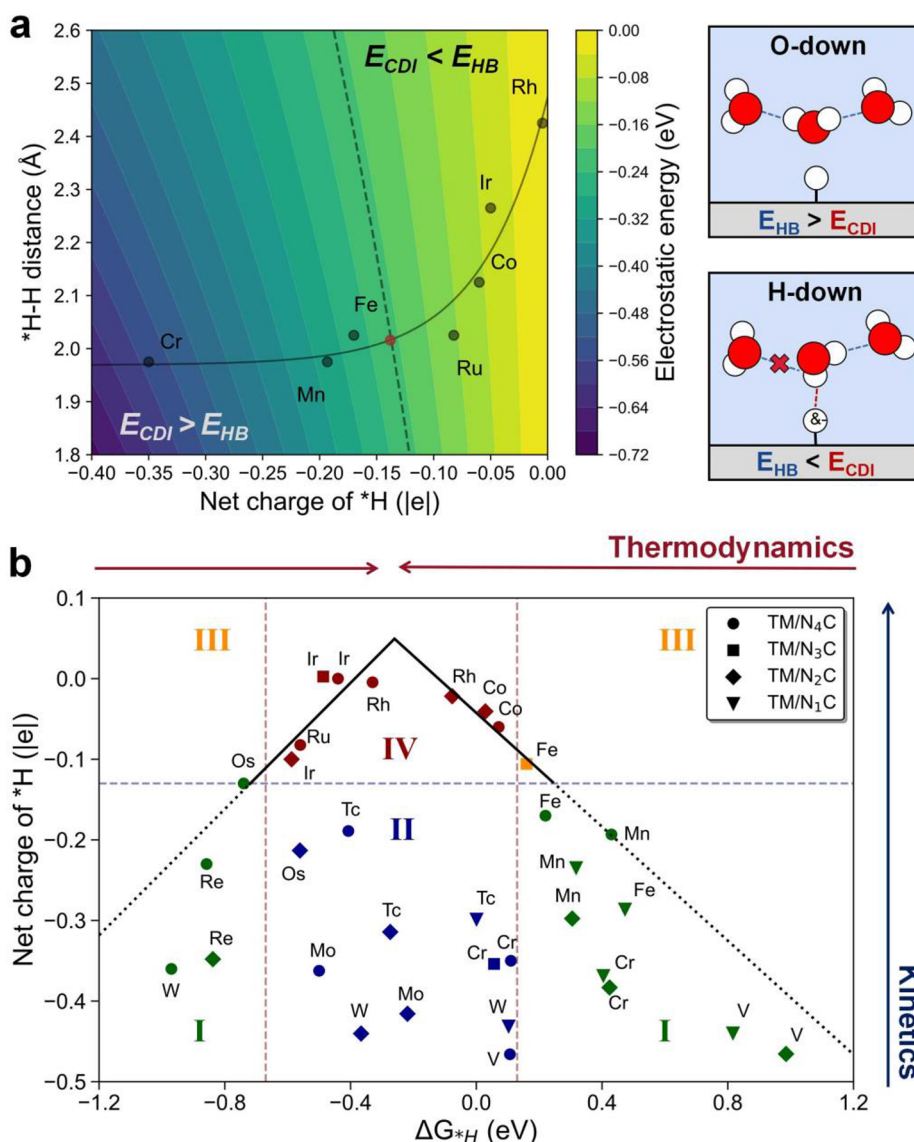
Figure 4. Design principles of TM/N$_x$C for acidic HER. (a) Three-dimensional volcano plot for the assessment of kinetic influence during Volmer reaction. The energy of charge−dipole interaction (E_{CDI}) is calculated via the *H···H distance and net charge of *H which are analyzed from AIMD simulations. The dash line refers to the energy of hydrogen bond which is derived from ref 50, and the solid line refers to the fitted line with exponential form. The picture on the right panel illustrates two kinds of final state on Volmer reaction ("O-down" type and "H-down" type). (b) Theoretical evaluation of the acidic HER activity on different TM/N$_x$C. Areas I, II, III, and IV indicate that the HER on TM/N$_x$C is both thermodynamically and kinetically limited, only kinetically limited, only thermodynamically limited, and highly active, respectively. The black line indicates the "volcano" relationship of ΔG_{*H} and net charge of *H, where the fitted data comes from area III and area IV.

spectra of all the four SAEs can be deconvoluted into a metal−N species (M−N), demonstrating that single metal atoms coordinate with adjacent nitrogen atoms via the M−N bonds and the N species in M−N is in the pyridinic form (Figure S12). Furthermore, quantitative structural parameters for all the four TM-based SAEs have been determined by least-squares Fourier transform extended X-ray absorption fine structure (FT-EXAFS) analysis, indicating four-coordinate TM centers with mean bond lengths of about 1.9−2.0 Å, which not only doubly verify the isolated atomic dispersion of TM species in SAEs but also confirm that the coordination environments of experimental samples are in accordance with those of simulation models (see Figure S16 and Table S3)

Then the HER performances of the four SAEs were evaluated in 0.1 M aqueous HClO$_4$ electrolyte on a rotating disk electrode (RDE). Figure 3c displays the polarization

curves, among which Rh/NC exhibits the best HER activity with the lowest onset potential and overpotential at the current density of 10 mA cm^{-2}. As another important criterion, the excellent stability of Rh/NC is also demonstrated by negligible voltage degradation of long-term durability test over 20 h (Figure S17) and little metal dissolution of only 1.86% in the recycled electrolyte. HER activity trend follows Rh/NC > Co/NC > Cr/NC > FeNC, and importantly, it should be noted that the HER activity of Fe/NC will be conversely better than that of Cr/NC at higher current densities (>20 mA cm^{-2}). This implies that there is a more pronounced kinetic limitation on the HER activity of Cr/NC evidenced by the measured Tafel slope which is as high as 157.5 mV dec^{-1} (Figure 3d). The lowest Tafel slope of Co/NC (99.1 mV dec^{-1}) indicates the kinetically favorable HER, matching well with the theoretical prediction that the energy barrier is nearly equal

to the free energy (Figure S7d). Besides, the Tafel slopes of all the four SAEs are close to 120 mV decade^{-1}, suggesting that the Volmer reaction is the rate-determining step (RDS) for all the studied catalysts, in good agreement with the theoretical assumption.[48] It is worth noting that the overall HER activity is also determined by Volmer step on many reported SAEs with TM/NC-like structure,[17,21,23,49] which reveals that relying on the thermodynamic and kinetic properties of the Volmer reaction alone could also give good predictions/insights for the design or optimization of SAEs to a large extent.

Catalyst Design Principle Based on Kinetic Descriptor. Considering the complexity of solid−liquid electrochemical interface, large spatial scale, and long-time scale needed to evaluate equilibrium properties, quantifying the charge−dipole interaction (CDI) between *H and neighboring H$_2$O by ab initio method is rather difficult. Here we estimate the electrostatic potential energy of CDI (E_{CDI}) for different TM/N$_4$C catalysts using an analytical equation:

$$E_{CDI} = \frac{q_i(-q_j)e^2}{4\pi\varepsilon_0} \frac{1}{|\mathbf{r_i} - \mathbf{r_j}|} + \frac{q_i(q_j)e^2}{4\pi\varepsilon_0} \frac{1}{|\mathbf{r_i} + \mathbf{P_j} - \mathbf{r_j}|}$$

where q_i, q_j and $\mathbf{r_i}$, $\mathbf{r_j}$ are the net charge and coordinates of *H and O atom of H$_2$O; $\mathbf{P_j}$ refers to the dipole vector of H$_2$O, and ε_0 refers to the relative permittivity of vacuum. In brief, the E_{CDI} could be estimated via the distance of *H···H and net charge of *H, which are derived from RDF analysis of AIMD simulation and Bader charge analysis, respectively. The estimations for various metal centers are presented in Table S4. Since the interaction between *H and interfacial water would partially disrupt the hydrogen bond network, it is also informative to compare the E_{CDI} and the energy of hydrogen bond (E_{HB}), which is approximately −0.21 eV from previous report.[50] As is shown in Figure 4a, if the CDI outcompetes the hydrogen bond between H$_2$O molecules, the configuration of H$_2$O would likely transform from "O-down" to "H-down" orientation during reaction; otherwise the interfacial H$_2$O would stay "O-down". For example, the E_{CDI} on Cr/N$_4$C, Mn/N$_4$C and Fe/N$_4$C are estimated to be −0.55 eV, −0.30 eV, and −0.26 eV, respectively, suggesting a "H-down" orientation of interfacial H$_2$O which is consistent with our RDF analysis and *H···O−H angle analysis from constrained MD simulations. In addition, an exponential relationship is fitted between the net charge on *H and the *H···H distance. In this case, the net charge on *H could work as a physical descriptor for the kinetics of Volmer reaction, and the intersection (net charge of *H = −0.13 |e|) of fitted line and E_{HB} marks the critical point beyond which the kinetic limitation is pronounced.

The coordination sphere engineering of TM/N$_x$C is an effective strategy to optimize the electrocatalytic performance at molecular level.[51−53] By plotting the kinetics descriptor (net charge of *H) versus the thermodynamics descriptor (ΔG_{*H}), we further investigated the properties of hydrogen adsorption on different TM/N$_x$C, in which the type of transition metal atom and the number of doped-N are changed, respectively (Figure 4b). Our study suggests that regulating the number of doped-N around the metal center, which can be achieved by controlling the concentration of N source or the metal precursor, can significantly alter the kinetics and thermodynamics. For example, by changing the number of doped N around the metal center from 2 to 4, the ΔG_{*H} on Cr/N$_x$C is increased by 0.29 eV, whereas on V/N$_x$C it is lowered by 0.88 eV. This modulation can be explained by the projected density

of states (PDOS) analysis (Figure S13), where the number of doped-N influences the electronic structure of central metal atom (the emerging 3d$_{z^2}$ orbital above the Fermi level on Cr/N$_2$C) and the orbital interaction between Cr 3d$_{z^2}$ orbital with H 1s orbital (the energy level overlap of 3d$_{z^2}$ and 1s orbitals on Cr/N$_4$C is about 0.50 eV lower than Cr/N$_2$C). The kinetics of Volmer reaction would be improved on Fe/N$_x$C if the number of doped N is regulated from 1 to 3, since the net charge of *H is positively increased ∼0.2 |e|. However, for the metals with low electronegativity, such as Cr, W, and V, the coordination engineering makes very little difference to kinetics, with the change in net charge of *H under within 0.1 |e| as the number of doped-N is varied.

Based on the understanding of the kinetics effects, we could classify the SAEs into four types by the extent of kinetic hindrance on them: types I, II, III, and IV (Figure 4b) represent the cases where HER is both thermodynamically (the ΔG_{*H} on SAEs are far from the optimal value) and kinetically limited (too hydridic due to net charge of *H < −0.13 |e|), only kinetically limited, only thermodynamically limited, and highly active (thermodynamically optimal and kinetically unhindered), respectively. Besides the Rh/N$_4$C and Co/N$_4$C which have been confirmed by electrochemical measurement, the Ir/N$_{2−4}$C, Ru/N$_4$C, Rh/N$_2$C, and Co/N$_2$C all fall into the type IV and are hence expected to also have good HER performance. Without the need of kinetic consideration, these SAEs (type III and type IV) follow the trend as in the traditional "volcano" plot, i.e., the HER activity could be solely evaluated by ΔG_{*H}.

To address the regions where the original activity volcano fails to describe, we extend the activity volcano relationships by incorporating an additional descriptor for kinetics, net charge of *H (Figure 4b). In cases where the hydrogen adsorption is too strong or too weak, the overall HER would be severely thermodynamically limited; thus the trends as in the traditional "volcano" plot still hold within this region. The SAEs near the extended volcano arms (dotted lines) would also follow the original trend since their kinetic and thermodynamic factors correlate, such as Mn/N$_4$C, Os/N$_4$C, etc. However, the original trend is intrinsically not applicable to the SAEs that are far from the extended volcano arms, especially the ones in region II (Cr/N$_4$C, V/N$_4$C, etc.), due to the decorrelated kinetic and thermodynamics properties. In other words, their Volmer reaction free energy are near-optimal, but their free energy barriers are unproportionally high. For such cases, only relying on the thermodynamics would result in a significant gap between theoretical estimations and experimental observations of the HER activity.

Such decorrelating behavior of reaction kinetics and thermodynamics may be present in other reactions alike, especially the ones that interacts strongly with solvent molecules. We would hence expect the activity volcano, and the underlying linear scaling relations, to be routinely broken on SAEs, which indeed opens up a much greater room for catalyst optimization. There are possible ways to reduce or eliminate the kinetic limitation, which include the following. (i) Electronic modulation of the single atom site. This includes coordination engineering of the SAEs (by controlled doping of the carbon matrix) or introduction of axial ligands to tune the acidity/hydridicity of the *H species. (ii) Interfacial interaction modulation. This can be achieved by functionalizing the catalyst surface with strong hydrogen bond donating or accepting groups or by adding structure making ions to the

electrolyte[54] to strengthen the interfacial hydrogen bond network and promote the O-down transition state configuration. Besides, although these design principles and suggestions mainly focus on enhancing the HER activity, it could still provide useful insights for the design of SAEs for hydrogen oxidation reaction (HOR) if the overall reaction kinetics is controlled by hydrogen desorption. In addition, we further analyze why the thermodynamic-only criterion is generally reliable for screening the transition metal electrocatalysts. It is probably due to the intrinsic differences between SAEs and transition metal electrocatalysts, such as properties of metal atoms and interfacial electric double layer. We therefore calculated the charge state of *H on noble metal surfaces with high experimental activity (Table S5). The near neutral *H on these metallic surface reveals that the kinetic obstruction aroused by charge-dipole interaction may not exist on these systems.

Finally, we also find that the charge state of the metal center in the nitrogen doped graphene (before H adsorption) and the valence electrons of the metal atom (in its atomic form) could correlate with the charge state of the adsorbed *H (Figure S18). This reveals that the proposed descriptor, i.e., the net charge of *H could be related to the intrinsic properties of SAEs and a precise descriptor which takes more physical properties into account could replace the H-charge descriptor. In addition to DFT calculations, other advanced techniques (e.g., machine learning method) may be helpful to achieve this idea in future studies.

CONCLUSIONS

In this work, we have employed ab initio molecular dynamics (AIMD) simulations and thermodynamic integration method with explicit solvation to explore the origin of kinetics bottleneck in acidic Volmer reaction on TM/N_4C single atom catalysts. We have identified an interfacial charge−dipole interaction between the adsorbed hydrogen species and interfacial water in its surroundings, which dictates the orientation of interfacial water during the Volmer reaction to be a descriptor for the kinetics of Volmer reaction on TM/N_4C single-atom catalysts. In particular, we shed light on the reason why the traditional screening strategy based on HER activity volcano fails for designing SAEs: Different metal centers lead to different hydricity of the key *H intermediate, which reshapes the free energy surface of the Volmer reaction and induces a phase transition-like reorientation of interfacial water configuration along the reaction profile, significantly raising the barriers for the systems with *H of weak hydricity. The presumed correlation between the thermodynamics and the kinetics by the traditional strategy, based on Sabatier principle and BEP relation, does not hold true on SAEs as a result.

Based on the understanding, our work incorporates kinetics considerations into the original activity volcano to extend its applicability, with ample discussions on where the original trend still holds (in regions where kinetics and thermodynamics correlate well) and where it would fail (in regions where they decorrelate). Designing principles are proposed on this extended model, with suggestions on the construction of optimal SAEs. Our findings also emphasize the critical role of local solvent environment around the intermediates, especially the phase transition-like reorientation of interfacial water induced by certain charged species, for exploring the catalytic mechanism, studying activity trends, and rational design of optimal electrocatalysts.

ASSOCIATED CONTENT

Supporting Information

The Supporting Information is available free of charge at https://pubs.acs.org/doi/10.1021/jacs.2c13418.

Figures S1−18, Tables S1−S6, original structure data, and input parameters (PDF)

AUTHOR INFORMATION

Corresponding Authors

Bin Liu − *School of Chemistry, Chemical Engineering and Biotechnology, Nanyang Technological University, Singapore 637459, Singapore; Department of Materials Science and Engineering, City University of Hong Kong, Hong Kong SAR 999077, China;* orcid.org/0000-0002-4685-2052; Email: liubin@ntu.edu.sg, bliu48@cityu.edu.hk

Yang-Gang Wang − *Department of Chemistry and Guangdong Provincial Key Laboratory of Catalysis, Southern University of Science and Technology, Shenzhen 518055 Guangdong, China;* orcid.org/0000-0002-0582-0855; Email: wangyg@sustech.edu.cn

Authors

Hao Cao − *Department of Chemistry and Guangdong Provincial Key Laboratory of Catalysis, Southern University of Science and Technology, Shenzhen 518055 Guangdong, China*

Qilun Wang − *School of Chemistry, Chemical Engineering and Biotechnology, Nanyang Technological University, Singapore 637459, Singapore*

Zisheng Zhang − *Department of Chemistry and Biochemistry, University of California, Los Angeles, California 90095, United States;* orcid.org/0000-0002-4370-4038

Hui-Min Yan − *Department of Chemistry and Guangdong Provincial Key Laboratory of Catalysis, Southern University of Science and Technology, Shenzhen 518055 Guangdong, China*

Hongyan Zhao − *Department of Chemistry and Guangdong Provincial Key Laboratory of Catalysis, Southern University of Science and Technology, Shenzhen 518055 Guangdong, China*

Hong Bin Yang − *School of Chemistry, Chemical Engineering and Biotechnology, Nanyang Technological University, Singapore 637459, Singapore;* orcid.org/0000-0002-7834-4706

Jun Li − *Department of Chemistry, Tsinghua University, Beijing 100084, China;* orcid.org/0000-0002-8456-3980

Complete contact information is available at:
https://pubs.acs.org/10.1021/jacs.2c13418

Author Contributions

¶H.C. and Q.W. contributed equally to this paper.

Notes

The authors declare no competing financial interest.

■ REFERENCES

(1) Chu, S.; Majumdar, A. Opportunities and Challenges for a Sustainable Energy Future. *Nature* **2012**, *488* (7411), 294−303.

(2) Jiao, Y.; Zheng, Y.; Jaroniec, M.; Qiao, S. Z. Design of Electrocatalysts for Oxygen- and Hydrogen-Involving Energy Conversion Reactions. *Chem. Soc. Rev.* **2015**, *44* (8), 2060−2086.

(3) Zhu, J.; Hu, L.; Zhao, P.; Lee, L. Y. S.; Wong, K. Y. Recent Advances in Electrocatalytic Hydrogen Evolution Using Nanoparticles. *Chem. Rev.* **2020**, *120* (2), 851−918.

(4) Shen, L.-f.; Lu, B.-a.; Li, Y.-y.; Liu, J.; Huang-fu, Z.-c.; Peng, H.; Ye, J.-y.; Qu, X.-m.; Zhang, J.-m.; Li, G.; Cai, W.-b.; Jiang, Y.-x.; Sun, S.-g. Interfacial Structure of Water as a New Descriptor of the Hydrogen Evolution Reaction. *Angew. Chem., Int. Ed.* **2020**, *59*, 22397.

(5) McCrum, I. T.; Koper, M. T. M. The Role of Adsorbed Hydroxide in Hydrogen Evolution Reaction Kinetics on Modified Platinum. *Nat. Energy* **2020**, *5* (11), 891−899.

(6) Zhu, S.; Qin, X.; Xiao, F.; Yang, S.; Xu, Y.; Tan, Z.; Li, J.; Yan, J.; Chen, Q.; Chen, M.; Shao, M. The Role of Ruthenium in Improving the Kinetics of Hydrogen Oxidation and Evolution Reactions of Platinum. *Nat. Catal.* **2021**, *4* (8), 711−718.

(7) Durst, J.; Siebel, A.; Simon, C.; Hasché, F.; Herranz, J.; Gasteiger, H. A. New Insights into the Electrochemical Hydrogen Oxidation and Evolution Reaction Mechanism. *Energy Environ. Sci.* **2014**, *7* (7), 2255−2260.

(8) Strmcnik, D.; Uchimura, M.; Wang, C.; Subbaraman, R.; Danilovic, N.; Van Der Vliet, D.; Paulikas, A. P.; Stamenkovic, V. R.; Markovic, N. M. Improving the Hydrogen Oxidation Reaction Rate by Promotion of Hydroxyl Adsorption. *Nat. Chem.* **2013**, *5* (4), 300−306.

(9) Trasatti, S. Work Function, Electronegativity, and Electrochemical Behaviour of Metals. III. Electrolytic Hydrogen Evolution in Acid Solutions. *J. Electroanal. Chem.* **1972**, *39* (1), 163−184.

(10) Sabatier, P. Hydrogénations et Déshydrogénations Par Catalyse. *Berichte der Dtsch. Chem. Gesellschaft* **1911**, *44* (3), 1984−2001.

(11) Nørskov, J. K.; Bligaard, T.; Logadottir, A.; Kitchin, J. R.; Chen, J. G.; Pandelov, S.; Stimming, U. Trends in the Exchange Current for Hydrogen Evolution. *J. Electrochem. Soc.* **2005**, *152* (3), J23.

(12) Seh, Z. W.; Kibsgaard, J.; Dickens, C. F.; Chorkendorff, I.; Nørskov, J. K.; Jaramillo, T. F. Combining Theory and Experiment in Electrocatalysis: Insights into Materials Design. *Science* **2017**, *355* (6321), eaad4998.

(13) Greeley, J.; Mavrikakis, M. Alloy Catalysts Designed from First Principles. *Nat. Mater.* **2004**, *3* (11), 810−815.

(14) Greeley, J.; Nørskov, J. K.; Kibler, L. A.; El-Aziz, A. M.; Kolb, D. M. Hydrogen Evolution over Bimetallic Systems: Understanding the Trends. *ChemPhysChem* **2006**, *7* (5), 1032−1035.

(15) Zhang, Q.; Guan, J. Single-Atom Catalysts for Electrocatalytic Applications. *Adv. Funct. Mater.* **2020**, *30* (31), 2000768.

(16) Zhao, X.; Levell, Z. H.; Yu, S.; Liu, Y. Atomistic Understanding of Two-Dimensional Electrocatalysts from First Principles. *Chem. Rev.* **2022**, *122* (12), 10675−10709.

(17) Jiao, Y.; Zheng, Y.; Davey, K.; Qiao, S. Z. Activity Origin and Catalyst Design Principles for Electrocatalytic Hydrogen Evolution on Heteroatom-Doped Graphene. *Nat. Energy* **2016**, *1* (10), 16130.

(18) Sabhapathy, P.; Shown, I.; Sabbah, A.; Raghunath, P.; Chen, J. L.; Chen, W. F.; Lin, M. C.; Chen, K. H.; Chen, L. C. Electronic Structure Modulation of Isolated Co-N4 Electrocatalyst by Sulfur for Improved PH-Universal Hydrogen Evolution Reaction. *Nano Energy* **2021**, *80*, 105544.

(19) Cheng, N.; Stambula, S.; Wang, D.; Banis, M. N.; Liu, J.; Riese, A.; Xiao, B.; Li, R.; Sham, T. K.; Liu, L. M.; Botton, G. A.; Sun, X. Platinum Single-Atom and Cluster Catalysis of the Hydrogen Evolution Reaction. *Nat. Commun.* **2016**, *7*, eaad4998.

(20) Fei, H.; Dong, J.; Arellano-Jiménez, M. J.; Ye, G.; Dong Kim, N.; Samuel, E. L. G.; Peng, Z.; Zhu, Z.; Qin, F.; Bao, J.; Yacaman, M. J.; Ajayan, P. M.; Chen, D.; Tour, J. M. Atomic Cobalt on Nitrogen-Doped Graphene for Hydrogen Generation. *Nat. Commun.* **2015**, *6*, 8668.

(21) Chen, W.; Pei, J.; He, C. T.; Wan, J.; Ren, H.; Zhu, Y.; Wang, Y.; Dong, J.; Tian, S.; Cheong, W. C.; Lu, S.; Zheng, L.; Zheng, X.; Yan, W.; Zhuang, Z.; Chen, C.; Peng, Q.; Wang, D.; Li, Y. Rational Design of Single Molybdenum Atoms Anchored on N-Doped Carbon for Effective Hydrogen Evolution Reaction. *Angew. Chemie - Int. Ed.* **2017**, *56* (50), 16086−16090.

(22) Di Liberto, G.; Cipriano, L. A.; Pacchioni, G. Role of Dihydride and Dihydrogen Complexes in Hydrogen Evolution Reaction on Single-Atom Catalysts. *J. Am. Chem. Soc.* **2021**, *143* (48), 20431−20441.

(23) Hossain, M. D.; Liu, Z.; Zhuang, M.; Yan, X.; Xu, G. L.; Gadre, C. A.; Tyagi, A.; Abidi, I. H.; Sun, C. J.; Wong, H.; Guda, A.; Hao, Y.; Pan, X.; Amine, K.; Luo, Z. Rational Design of Graphene-Supported Single Atom Catalysts for Hydrogen Evolution Reaction. *Adv. Energy Mater.* **2019**, *9* (10), 1803689.

(24) Li, H.; Wang, G.; Zhang, F.; Zou, L.; Zou, Z.; Yang, H. An Atomically Dispersed Pt Catalyst Anchored on an Fe/N/C Support for Enhanced Hydrogen Evolution Reaction. *J. Phys. Chem. C* **2020**, *124* (22), 11760−11766.

(25) Chen, J.-W.; Zhang, Z.; Yan, H.-M.; Xia, G.-J.; Cao, H.; Wang, Y.-G. Pseudo-Adsorption and Long-Range Redox Coupling during Oxygen Reduction Reaction on Single Atom Electrocatalyst. *Nat. Commun.* **2022**, *13* (1), 1734.

(26) Cheng, T.; Wang, L.; Merinov, B. V.; Goddard, W. A. Explanation of Dramatic PH-Dependence of Hydrogen Binding on Noble Metal Electrode: Greatly Weakened Water Adsorption at High PH. *J. Am. Chem. Soc.* **2018**, *140* (25), 7787−7790.

(27) Le, J.-B.; Fan, Q.-Y.; Li, J.-Q.; Cheng, J. Molecular Origin of Negative Component of Helmholtz Capacitance at Electrified Pt(111)/Water Interface. *Sci. Adv.* **2020**, *6* (41), eabb1219.

(28) Zhao, X.; Liu, Y. Unveiling the Active Structure of Single Nickel Atom Catalysis: Critical Roles of Charge Capacity and Hydrogen Bonding. *J. Am. Chem. Soc.* **2020**, *142* (12), 5773−5777.

(29) Cao, H.; Zhang, Z.; Chen, J.-W.; Wang, Y.-G. Potential-Dependent Free Energy Relationship in Interpreting the Electrochemical Performance of CO 2 Reduction on Single Atom Catalysts. *ACS Catal.* **2022**, *12* (11), 6606−6617.

(30) Resasco, J.; Abild-Pedersen, F.; Hahn, C.; Bao, Z.; Koper, M. T. M.; Jaramillo, T. F. Enhancing the Connection between Computation and Experiments in Electrocatalysis. *Nat. Catal.* **2022**, *5* (5), 374−381.

(31) Kohn, W.; Sham, L. J. Self-Consistent Equations Including Exchange and Correlation Effects. *Phys. Rev.* **1965**, *140* (4A), A1133−A1138.

(32) Kresse, G.; Furthmüller, J. Efficient Iterative Schemes for Ab Initio Total-Energy Calculations Using a Plane-Wave Basis Set. *Phys. Rev. B - Condens. Matter Mater. Phys.* **1996**, *54* (16), 11169−11186.

(33) Perdew, J. P.; Burke, K.; Ernzerhof, M. Generalized Gradient Approximation Made Simple. *Phys. Rev. Lett.* **1996**, *77* (18), 3865−3868.

(34) Mathew, K.; Sundararaman, R.; Letchworth-Weaver, K.; Arias, T. A.; Hennig, R. G. Implicit Solvation Model for Density-Functional Study of Nanocrystal Surfaces and Reaction Pathways. *J. Chem. Phys.* **2014**, *140* (8), 084106.

(35) Nørskov, J. K.; Rossmeisl, J.; Logadottir, A.; Lindqvist, L.; Kitchin, J. R.; Bligaard, T.; Jónsson, H. Origin of the Overpotential for Oxygen Reduction at a Fuel-Cell Cathode. *J. Phys. Chem. B* **2004**, *108* (46), 17886−17892.

(36) Vandevondele, J.; Krack, M.; Mohamed, F.; Parrinello, M.; Chassaing, T.; Hutter, J. Quickstep: Fast and Accurate Density Functional Calculations Using a Mixed Gaussian and Plane Waves Approach. *Comput. Phys. Commun.* **2005**, *167* (2), 103−128.

(37) Martyna, G. J.; Klein, M. L.; Tuckerman, M. Nosé-Hoover Chains: The Canonical Ensemble via Continuous Dynamics. *J. Chem. Phys.* **1992**, *97* (4), 2635−2643.

(38) Hoover, W. G. Canonical Dynamics: Equilibrium Phase-Space Distributions. *Phys. Rev. A* **1985**, *31* (3), 1695−1697.

(39) Grimme, S.; Ehrlich, S.; Goerigk, L. Effect of the Damping Function in Dispersion Corrected Density Functional Theory. *J. Comput. Chem.* **2011**, *32* (7), 1456−1465.

(40) Carter, E. A.; Ciccotti, G.; Hynes, J. T.; Kapral, R. Constrained Reaction Coordinate Dynamics for the Simulation of Rare Events. *Chem. Phys. Lett.* **1989**, *156* (5), 472−477.

(41) Sprik, M.; Ciccotti, G. Free Energy from Constrained Molecular Dynamics. *J. Chem. Phys.* **1998**, *109* (18), 7737−7744.

(42) Le, J.-B.; Yang, X.-H.; Zhuang, Y.-B.; Jia, M.; Cheng, J. Recent Progress toward Ab Initio Modeling of Electrocatalysis. *J. Phys. Chem. Lett.* **2021**, *12*, 8924−8931.

(43) Kronberg, R.; Laasonen, K. Reconciling the Experimental and Computational Hydrogen Evolution Activities of Pt(111) through DFT-Based Constrained MD Simulations. *ACS Catal.* **2021**, *11* (111), 8062−8078.

(44) Chan, K.; Nørskov, J. K. Potential Dependence of Electrochemical Barriers from Ab Initio Calculations. *J. Phys. Chem. Lett.* **2016**, *7* (9), 1686−1690.

(45) Chan, K.; Nørskov, J. K. Electrochemical Barriers Made Simple. *J. Phys. Chem. Lett.* **2015**, *6* (14), 2663−2668.

(46) Yang, H.; Hung, S. F.; Liu, S.; Yuan, K.; Miao, S.; Zhang, L.; Huang, X.; Wang, H. Y.; Cai, W.; Chen, R.; Gao, J.; Yang, X.; Chen, W.; Huang, Y.; Chen, H. M.; Li, C. M.; Zhang, T.; Liu, B. Atomically Dispersed Ni(i) as the Active Site for Electrochemical CO2 Reduction. *Nat. Energy* **2018**, *3* (2), 140−147.

(47) Wang, Q.; Xu, C. Q.; Liu, W.; Hung, S. F.; Bin Yang, H.; Gao, J.; Cai, W.; Chen, H. M.; Li, J.; Liu, B. Coordination Engineering of Iridium Nanocluster Bifunctional Electrocatalyst for Highly Efficient and PH-Universal Overall Water Splitting. *Nat. Commun.* **2020**, *11* (1), 4246.

(48) Conway, B. E.; Tilak, B. V. Interfacial Processes Involving Electrocatalytic Evolution and Oxidation of H2, and the Role of Chemisorbed H. *Electrochim. Acta* **2002**, *47* (22−23), 3571−3594.

(49) da Silva Freitas, W.; Pico, P. P. M.; D'Epifanio, A.; Mecheri, B. Nanostructured Fe-N-C as Bifunctional Catalysts for Oxygen Reduction and Hydrogen Evolution. *Catalysts* **2021**, *11* (12), 1525.

(50) Emamian, S.; Lu, T.; Kruse, H.; Emamian, H. Exploring Nature and Predicting Strength of Hydrogen Bonds: A Correlation Analysis Between Atoms-in-Molecules Descriptors, Binding Energies, and Energy Components of Symmetry-Adapted Perturbation Theory. *J. Comput. Chem.* **2019**, *40* (32), 2868−2881.

(51) Lu, B.; Liu, Q.; Chen, S. Electrocatalysis of Single Atom Sites: Impacts of Atomic Coordination. *ACS Catal.* **2020**, *10* (14), 7584−7618.

(52) Patniboon, T.; Hansen, H. A. Acid-Stable and Active M−N−C Catalysts for the Oxygen Reduction Reaction: The Role of Local Structure. *ACS Catal.* **2021**, *11* (21), 13102−13118.

(53) Xu, H.; Cheng, D.; Cao, D.; Zeng, X. C. A Universal Principle for a Rational Design of Single-Atom Electrocatalysts. *Nat. Catal.* **2018**, *1* (5), 339−348.

(54) Mähler, J.; Persson, I. A Study of the Hydration of the Alkali Metal Ions in Aqueous Solution. *Inorg. Chem.* **2012**, *51* (1), 425−438.

(55) Choi, C. H.; Lim, H. K.; Chung, M. W.; Chon, G.; Ranjbar Sahraie, N.; Altin, A.; Sougrati, M. T.; Stievano, L.; Oh, H. S.; Park, E. S.; Luo, F.; Strasser, P.; Dražić, G.; Mayrhofer, K. J. J.; Kim, H.; Jaouen, F. The Achilles' Heel of Iron-Based Catalysts during Oxygen Reduction in an Acidic Medium. *Energy Environ. Sci.* **2018**, *11* (11), 3176−3182.

🕮 Recommended by ACS